Plasma- assisted liquid-based growth of g-C$_3$N$_4$/Mn$_2$O$_3$ p-n heterojunction with tunable valence band for photoelectrochemical application

Yanmei Zheng [a], Qiushi Ruan [a], JingXuan Ren [a], Xinli Guo [a,*], Yong Zhou [b], Boye Zhou [b], Qiang Xu [a], Qiuping Fu [a], Shaohua Wang [a], Ying Huang [c,*]

[a] *Jiangsu Key Laboratory of Advanced Metallic Materials, School of Materials Science and Engineering, Southeast University, Nanjing 211189, China*
[b] *School of Physics, Jiangsu Key Laboratory of Nanotechnology, Eco-materials and Renewable Energy Research Center, National Laboratory of Solid State Microstructures, Collaborative Innovation Center of Advanced Microstructures, Nanjing University, Nanjing, China*
[c] *School of Energy and Environment, Southeast University, Nanjing 210096, China*

ARTICLE INFO

ABSTRACT

The practical application of graphitic carbon nitride (g-C$_3$N$_4$, CN) is restricted by its low photocatalytic activity and difficult recycling. Herein, we report a CN/Mn$_2$O$_3$ p-n heterojunction grown by a plasma-assisted liquid-based method using a special precursor complex of melamine-cyanuric acid supramolecular on fluorine-doped tin oxide (FTO) substrate. The as-grown CN/Mn$_2$O$_3$/FTO p-n heterojunction exhibits a significantly enhanced photoelectrochemical performance with a photocurrent density of 25 μA/cm^2 compared with its powder form (0.9 μA/cm^2) formed by common drop coating method , and a tunable valence band (VB) with excellent mechanical strength which is benefit for photocatalytic oxidation reaction and recovery. The formation of CN/Mn$_2$O$_3$/FTO p-n heterojunction can promote the transfer of photoelectrons due to an internal electric field at the interface of p-n junction, leading to the accumulation of electrons and holes in the VB of CN and conduction band (CB) of Mn$_2$O$_3$. The results have shed a light on promoting the practical application of CN, and the developed plasma-assisted liquid-based growth method can be extended to the preparation of other type of functional heterojunctions.

1. Introduction

As a promising alternative to alleviate current global energy and environmental problems, photoelectrochemical (PEC) technology has attracted great interest in the past decades.[1–3] However, PEC technology is still limited by the lack of efficient photocatalysts for practical applications.[4] This has inspired considerable research on photocatalysts in pursuit of low cost, reproducibility, and suitable redox and oxidation potentials for water splitting. [5].

Recently, CN has drawn increasing interesting as a photoelectrode for PEC water splitting, PEC cell, CO$_2$ reduction, and environmental remediation due to its high visible-light-response, remarkable chemical and thermal stability.[6–10] Considerable researches have been done to modified the chemical, optical and electronic properties of CN, involving the formation of heterojunction, metal/nonmetal doping, plasma surface treatment and introduction of C and/or N vacancy etc. [11–15] Nevertheless, most of the modified methods of CN are normally based on thermal condensation to afford CN powder, which suffers from

a complex collection step resulting a hurdle for the real application. [16–18] To date, synthesis of CN powder photoelectrode has been mainly achieved by the common deposition methods such as screen printing, drop coating and spin coating, which normally lead to weak adhesion and poor CN coverage on the substrate FTO or indium tin oxide (ITO). Thus, various attempts have been made to improve the adhesion strength between CN and substrate, such as solid-state deposition, chemical vapor deposition and thermal vapor condensation etc. [19–21] However, these methods can only produce a rather thin CN layers, resulting in low light absorption, poor conductivity, weak photocurrent, and making CN films insufficient to act as active layers in photoelectrochemical cells or photovoltaic devices. Furthermore, it is difficult to control the thickness and uniformity of CN films deposited by these methods. Therefore, it is important and urgent to develop an effective method to prepare CN photoelectrodes with tunable thickness and good adhesion strength. In addition, manganese oxides, particularly the Mn$_2$O$_3$ have been recently employed as photocatalysts to enhance light absorption and charge separation due to their narrow bandgap and

---

high response.[22–24] Many of the PEC water splitting studies suggest that the importance of Mn^{3+} ions in the evolution of O_2 from water are attributed to the exceptional electrochemical oxygen evolution reaction (OER) activity.[25,26] More attractively, the combination of CN and Mn_2O_3 will be a tailor-designed photocatalyst to overcome the limit of the high recombination of photocarriers of pure CN.[27] Zhao et.al developed an innovative magnetic field enhanced 3D/2D $Mn_2O_3/g\text{-}C_3N_4$ photocatalytic system for denitrification from NO_3^--N and NH_4^+-N contaminated water. [28] However, there is still the problem that $Mn_2O_3/g\text{-}C_3N_4$ in powder form is difficult to recover, which sets up obstacles for practical application. Therefore, growing high-performance photocatalysts directly on substrates is a challenging but valuable research. But up to now, there are still no report about the liquid-based growth of $CN/Mn_2O_3/FTO$ p-n heterojunction for PEC water splitting. The construction of heterostructures with CN and Mn_2O_3 has been demonstrated as an effective method for improving PEC performance by enhancing charge separation at the interface. [11].

Herein, we report a plasma-assisted liquid-based growth of $CN/Mn_2O_3/FTO$ p-n heterojunction using the precursor complex of melamine-cyanuric acid supramolecular (MCS) on FTO substrate. The as-grown $CN/Mn_2O_3/FTO$ p-n heterojunction forms an internal electric field at the contact interface of p-n heterojunction, which can promote the transfer of photoelectrons to enhance photoelectrochemical performance. The tunable VB and excellent mechanical strength are benefit for photocatalytic oxidation reaction and recovery.

2. Experimental section

2.1. Plasma-assisted liquid-based growth of CN/Mn₂O₃/FTO p-n heterojunction

2.5 g melamine and 2.55 g cyanuric acid powders were dissolved in 10 ml of concentrated sulfuric acid (H_2SO_4) under stirring to obtain colloid. Then an amount of $KMnO_4$ was added into the obtained colloid hold in the ice bath for 1 h. The mixed colloid was heated at 35 ℃ for 2 h and 98 ℃ for 90 min, respectively. After cooling to room temperature, 20 ml of H_2O_2 was dropwise added to remove residual $KMnO_4$ and to get MCS. The as-prepared MCS were then added in 50 ml H_2O, centrifuged and dried at 80 ℃ for 48 h followed by a H_2 plasma treatment at a hydrogen flow rate of 30 sccm, 400 ℃ for 90 min and a pressure of 150 Pa to obtain CN/Mn_2O_3 p-n heterojunction. For practical PEC application, the above process was performed on a FTO substrate ($20 \times 20 \times 2.2$ mm³, 10 Ωsq⁻¹) to grow CN/Mn_2O_3 p-n heterojunction on FTO substrate ($CN/Mn_2O_3/FTO$). The obtained samples were labeled as $CN/Mn_2O_3/FTO\text{-}x$ (x = 0.25, 0.5, 0.75 or 1, corresponding to the mass of $KMnO_4$). For comparison, CN were also directly grown on FTO (CN/FTO) by the above process without adding $KMnO_4$.

2.2. Characterizations

Scanning electron microscopy (SEM, FEI Inspect F50) and Transmission electron microscopy (TEM, Titan 80–300) were used to study the morphologies and microstructures of samples. X-ray diffraction (XRD)-patterns were measured on a Bruker D8-Discover instrument using Cu-K$_\alpha$ radiation. The Brunauer-Emmett-Teller (BET, ASAP 2020) surface area was determined by nitrogen adsorption desorption isotherm. Fourier transform infrared spectroscopy (FTIR, Nicolet 5700 Fourier-IR spectrometer) was used to study the characterization of compounds. Thermal gravimetry (TG) and differential scanning calorimeter (DSC) were recorded on STA449 F3, Netzsch in nitrogen flow with a heating rate of 10 ℃/min. Electron paramagnetic resonance (EPR, Bruker A300) was measured by a digital X-band spectrometer. X-ray photoelectron microscope (XPS, PHI 500)-patterns were taken on Thermo Scientific Escal AB 250Xi. UV–vis absorbance spectra were measured by a Shimadzu UV-2550 UV–vis spectrometer. The photoluminescence (PL) spectra were determined using an Xe lamp as

excitation source. The in-situ XPS spectra (Thermo SCIENTIFIC ESCA-LAB 250Xi) were recorded under in-situ UV light irradiation for 10 min using xenon lamp by.

2.3. Photoelectrochemical measurement

Photoelectrochemical measurement were performed using an electrochemical workstation (CHI660E, Shanghai, China) under a three-electrode system. A platinum foil and saturated Ag/AgCl were used as counter electrode and reference electrode, respectively. The samples of $CN/Mn_2O_3/FTO$ and CN/FTO were directly used as working photoelectrode. For comparison, the corresponding powder photocatalyst CN/Mn_2O_3 was prepared by drop-coating and used as the working photoelectrode. The tests were conducted by using 0.1 M Na_2SO_4 solution and a 300 W xenon lamp (PLS-SXE 300D/300DUV, Beijing Perfect light) in an irradiation reaction vessel.

3. Results and discussion

3.1. Growth and characterization of CN/Mn₂O₃/FTO p-n heterojunction

The plasma-assisted liquid-based growth of $CN/Mn_2O_3/FTO$ p-n heterojunction is schematically shown in Fig. 1(a). The MCS powder was put on FTO substrate and then treated in H_2 plasma at 400 ℃ for 90 min under 150 Pa. When the heating temperature is near to the boiling point of H_2SO_4 (338 ℃), the hydrogen bonds of MCS start to break and form a liquid phase in which the Mn ions are dissolved and dispersed atomically. The liquid mixture become metastable due to the strong oxidizing of H_2SO_4, and the free-moving of Mn ions forms Mn_2O_3 with oxygen ions. Moreover, under the high energy H_2 plasma bombardment, the N atoms are moved from C-N=C and promote the generation of NH_3, which is conducive to the formation of porous structure. When the heating temperature exceeds the boiling point of H_2SO_4, the mixture with a hollow 3D structure is formed due to the release of NH_3 and low pressure.[19,29] The liquid-phase of the metastable state closely contact with the surface of the substrate, resulting in a good cycling performance which can keep stable after having been immersed in deionized water for a week as shown in Fig. S1(a) (Supporting information). The as-grown $CN/Mn_2O_3/FTO$ p-n heterojunction shows excellent mechanical strength which can support the weight of more than 1000 times of its own weight (See supporting information, Fig. S1(b)). For the PEC electrodes application, it is very important and a challenge to prepare PEC electrodes with a controllable thickness for optimizing charge transport. Fig. S1(c) shows the prepared $CN/Mn_2O_3/FTO$ p-n heterojunction PEC electrodes with different thicknesses by adjusting the parameters of pressure and the dosage of MCS. PEC electrodes with suitable thin layers can more easily separate charge carriers and transport them to the backside current collector, resulting in excellent photocurrent. Interesting, the arbitrary-scale 3D structures of CN/Mn_2O_3 p-n heterojunction can be formed without using any template during the synthesis process (Supporting information Fig. S1(d)), Such macroscopic 3D structural photocatalyst with better recovery properties and mechanical strength is suitable for the industrial and practical applications, such as photocatalytic degradation of pollutants, water splitting and H_2O_2 production.

It is worth mentioned that the critical factor to the plasma-assisted liquid-based growth method is the metastable colloid, which can be observed on the surface of MCS as shown in Fig. 1(b). The metastable colloid is prone to hydrolyze, thus the color of MCS can be immediately changed from brown to white when adding deionized water as shown in Fig. S2(a) (Supporting information). Meanwhile, the metastable colloid was disappeared after hydrolysis, which can be evidenced by the SEM images and photos in Fig. S2(b)-(e) (Supporting information). However, as shown in Fig. S3 (Supporting information), white MCS obtained after hydrolysis cannot form 3D structure photocatalyst under the same process, which further indicates that the metastable colloid is a critical
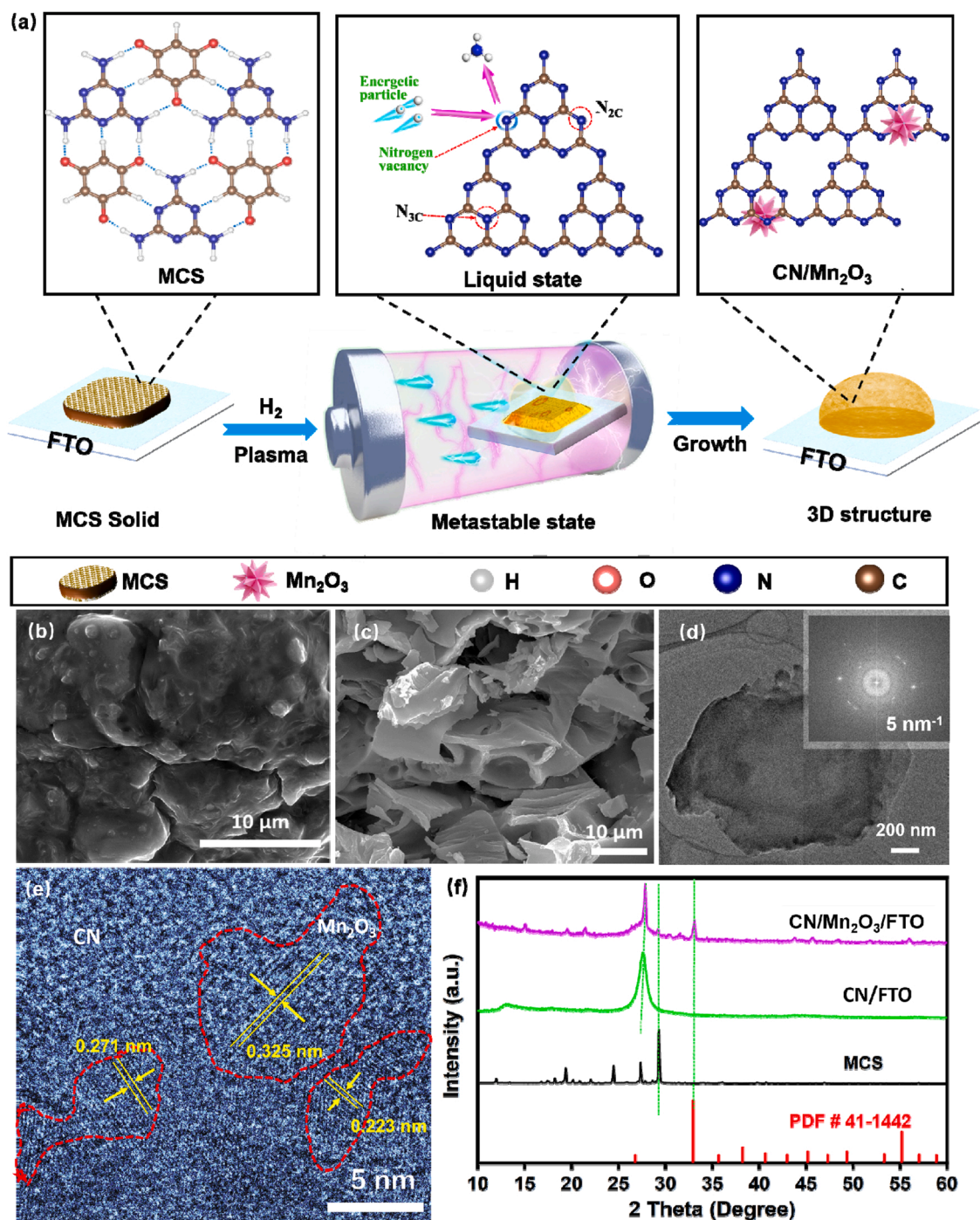
Fig. 1. (a) Schematically shown the process of plasma-assisted liquid-based growth of CN/Mn$_2$O$_3$/FTO p-n heterojunction; SEM images of (b) MCS and (c) CN/Mn$_2$O$_3$/FTO at different magnification; (d) and (e) High-resolution TEM images of CN/Mn$_2$O$_3$/FTO; (e) XRD patterns of the as-prepared samples.

factor to the liquid-based growth of macroscopic porous structure CN. Moreover, the layered and porous morphology of CN/Mn$_2$O$_3$/FTO (Fig. 1(c)) can provide large specific surface area. Compared with the specific surface area of CN/FTO (4.89 m^{2}g^{-1}), the CN/Mn$_2$O$_3$/FTO has a higher specific surface area (10.97 m^{2}g^{-1}) (Table S1, Fig. S4, Supporting information).

The TEM images were used to investigate the formation of CN/Mn$_2$O$_3$/FTO heterojunction. The Mn$_2$O$_3$ is constructed by small particles containing crystal diffraction spots (Fig. 1(d)). The high-resolution TEM image Fig. 2(e) indicates that Mn$_2$O$_3$ with defined lattice fringes of 0.223 nm, 0.271 nm and 0.352 nm, corresponding to (111), (222) and (002), respectively [30]. There is no obvious interface between CN and

Mn$_2$O$_3$ due to the liquid-based growth. Fig. 1(f) shows the XRD patterns of CN/Mn$_2$O$_3$/FTO, CN/FTO and MCS. The samples of CN/Mn$_2$O$_3$/FTO and CN/FTO show the same peak at 27.4° which can be assigned to the (002) plane of CN [31]. The dominate peak at 32.9° can be assigned to the (222) plane of Mn$_2$O$_3$ [30]. The FTIR spectra of CN/Mn$_2$O$_3$/FTO and CN/FTO show the same curves in Fig. 2(a). The strong absorption bands located at 1200–1700 cm^{-1} represent the typical stretching of CN heterocycles. The peak at 810 cm^{-1} is assigned to the characteristic breathing mode of the triazine units. The sharp peak at 603 cm^{-1} corresponds to the transverse-optical modes in stretching vibration of Mn-O in Mn$_2$O$_3$ [28], indicating the successful formation of CN/Mn$_2$O$_3$/FTO p-n heterojunction.
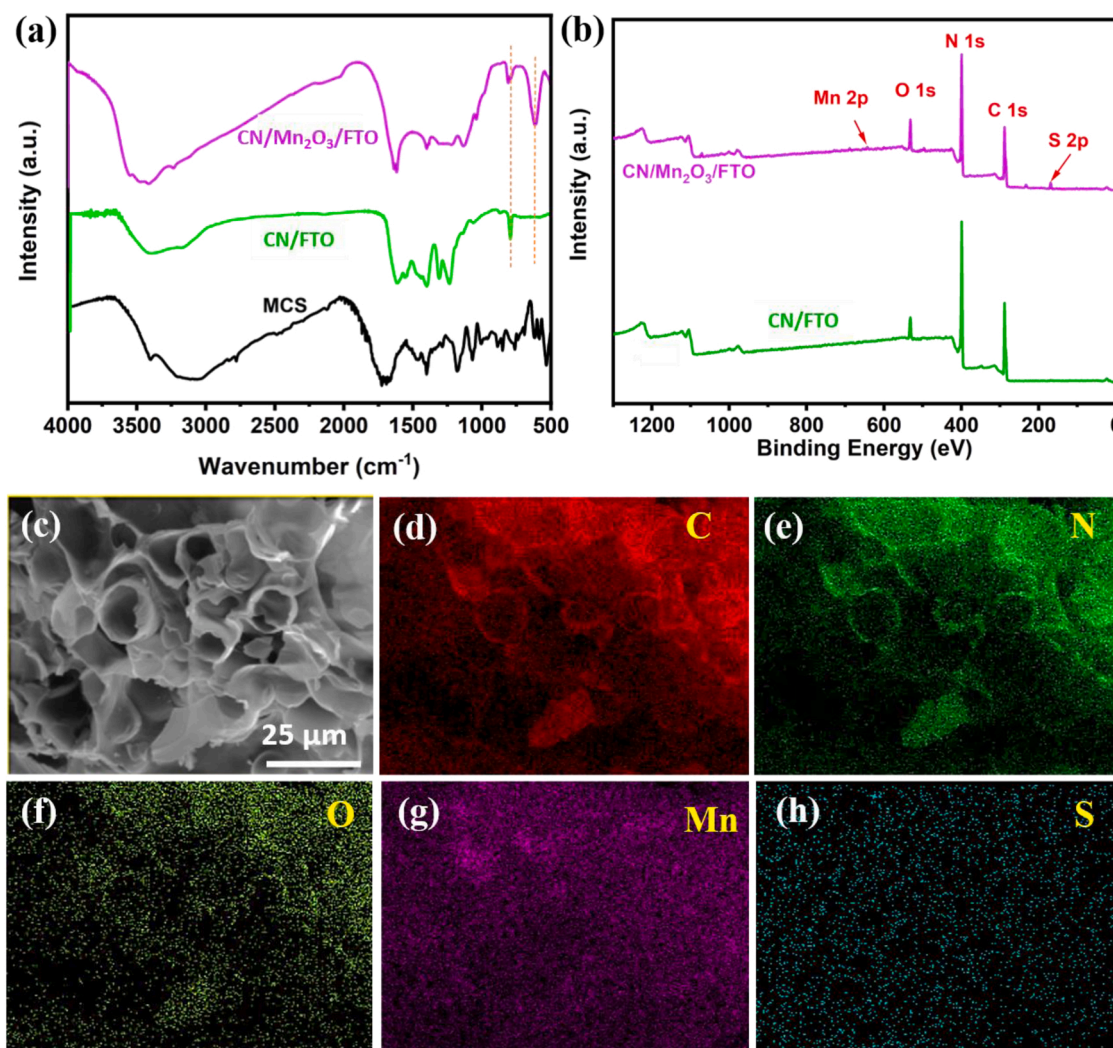
Fig. 2. (a) FTIR spectra of CN/Mn$_2$O$_3$/FTO, CN/FTO and MCS, (b) XPS survey spectra of CN/Mn$_2$O$_3$/FTO and CN/FTO, (c)-(h) EDX mapping of C (red), N (green), O (yellow), Mn (pink) and S (blue) of CN/Mn$_2$O$_3$/FTO.

In Fig. 2(b), the signals of C 1 s, N 1 s, O 1 s S 2p and Mn 2p are observed, which further indicates the existence of Mn$_2$O$_3$. Fig. 2(c)-(h) shows the SEM image of CN/Mn$_2$O$_3$/FTO and the corresponding elemental mapping of C, N, O, Mn, S elements uniformly dispersed on the surface of CN/Mn$_2$O$_3$/FTO, indicating the formation of CN/Mn$_2$O$_3$ heterojunction. The presence of S element should be attributed to the introduction of H$_2$SO$_4$, resulting in residual SO$_3^{2-}$/SO$_4^{2-}$ as evidenced by the S 2p XPS spectrum analysis (Fig. S5, Supporting information).

As shown in Fig. 3(a), to understand the plasma-assisted liquid-based growth process, the MCS precursor was put into a sealed quartz tube heated with H$_2$ fire. The solid MCS becomes a liquid phase when heated to its melting point. Meanwhile CN is formed accompanied by the release of NH$_3$ bubbles during the heating process. The white powder and red droplets on the inner surface of the tube are assigned to incompletely polymerized monomers and Mn$_2$O$_3$ dissolved in H$_2$SO$_4$, respectively. The thermal properties of MCS were investigated by TG and DSC as shown in Fig. 3(b). The MCS had almost no mass lose until 215 ℃. While the big mass loss was observed at 288.3 ℃, when the light brown powder turned to liquid accompanied by the release of NH$_3$ bubbles [32]. Another big mass loss occurred at 336.6 ℃, which can be assigned to the boiling of H$_2$SO$_4$ (boiling point: 338 ℃). By the results of DSC and SEM, it is reasonable to speculate that the component of colloid is attributed to H$_2$SO$_4$, which play an important role in the plasma-assisted liquid-based growth process. As we mentioned before,

the metastable colloid is considered as the critical factor to the plasma-assisted liquid-based growth, which provide close interface combination with the entire surface of the substrate, rather than the loose solid particles with gaps and poor contact with the substrate.[33] It can be distributed smoothly and continuously on the whole surface of the substrate.[21] The yellow powder on the inner surface of the quartz tube should be the result of Mn$_2$O$_3$. Therefore, the liquid-based growth of CN/Mn$_2$O$_3$/FTO photoelectrode could effectively reduce the interfacial effects[34]. In order to form hollow porous structure and macroscopic 3D structure as well as nitrogen vacancy, the H$_2$ plasma was employed [35]. Fig. 3(c) shows the EPR results of the CN/Mn$_2$O$_3$/FTO samples, which indicates the existence of nitrogen vacancy. There is an obvious Lorentz centerline near g= 2.003 of CN/Mn$_2$O$_3$/FTO, which corresponds to the unpaired electrons formed by sp^2 carbon atoms in aromatic ring due to the loss of partial nitrogen atom [36,37]. To investigate the surface chemical state of CN/Mn$_2$O$_3$/FTO more detail, the XPS high-resolution spectroscopy was employed. In C 1 s XPS spectrum (Fig. 3(d)), it can be fitted into three peaks that were C-C (284.8 eV), C-NH$_x$ (286.5 eV) and N=C-N (288.3 eV). The area ratio of the three peaks were similar for CN/FTO and CN/Mn$_2$O$_3$/FTO summarized in Table S2 (Supporting information), indicating that the carbon lattice site of CN did not be destroyed. In Fig. 3(e), the N 1 s XPS spectrum can be deconvoluted into three peaks which located at 401.1 eV, 399.9 eV and 398.6 eV assigned to C-NH$_x$, N-(C)$_3$ and C-N=C (N$_2$ $_C$),
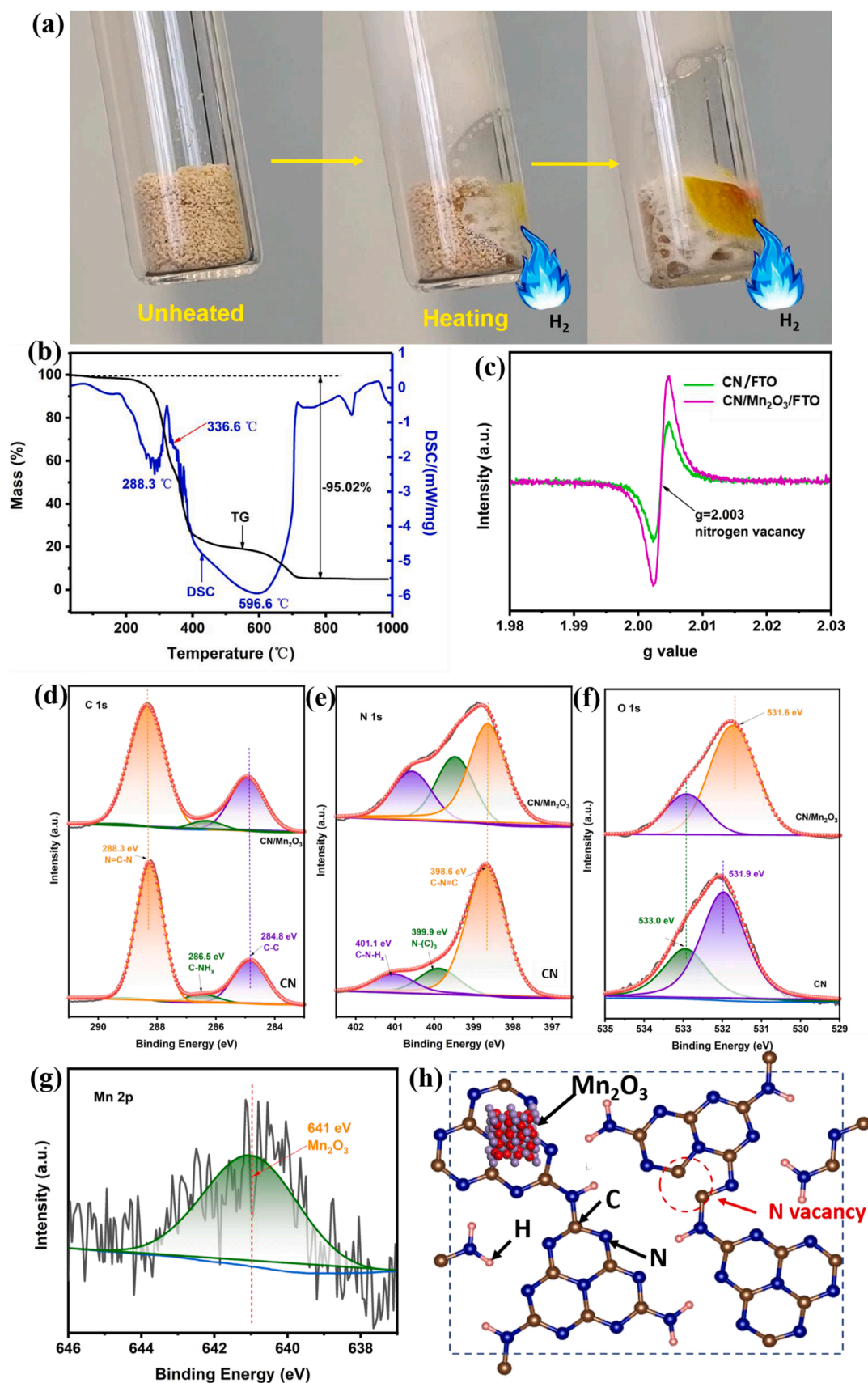
Fig. 3(. a) Phase transition of the MCS precursor in a sealed quartz tube using the tube sealing machine; (b) TG/DSC curves of the MCS; (c) EPR spectra of CN/Mn$_2$O$_3$/FTO and CN/FTO; (d)-(g) The XPS spectra and (h) the structure model of CN/Mn$_2$O$_3$/FTO.

respectively.

In order to further clarify the change of each bonding state caused by H_2 plasma treatment, a detailed analysis of the N 1 s spectra was conducted, which are summarized in Table S3 (Supporting information). Obviously, the area ratio of C=N − C (N_{2C}) reduces from 8.0 for CN/FTO to 2.4 for CN/Mn_2O_3/FTO, indicating the construction of N_{2C} vacancies, which is consistent with the results of EPR. Notably, compared to CN/FTO, the area ratio of N − C_3 (N_{3C}) for CN/Mn_2O_3/FTO is basically no change, further suggesting the nitrogen vacancies located at N_{2C} sites but not N_{3C} site. Moreover, the high-resolution O 1 s XPS spectrum (Fig. 3(f)) of CN/FTO can be fitted into two peaks at 531.9 eV and 533.0 eV, which are assigned to C=O/C-OH (the incompletely polymerized cyanuric acid) and absorbed water molecules, respectively. Whereas, a new generation peak located at 531.6 eV for CN/Mn_2O_3/FTO should be assigned to Mn-O bonds. Meanwhile, the high-resolution

spectra of Mn 2p shows one peak located at 641 eV is assigned to Mn_2O_3. Combined the above-mentioned XPS spectra, EPR with FT-IR spectra, especially the XRD, it can be concluded that the CN/Mn_2O_3/FTO heterojunction can be construction by the liquid-based growth, which lead less interface effect and more nitrogen vacancies. Thus, the model structure of CN/Mn_2O_3/FTO p-n heterojunction is showed in Fig. 3(h). Under the H_2 plasma, the high energy particles bombarded the N_{2C} lattice sites to form vacancies, accompanied by spilling of NH_3.[38] Meanwhile, the liquid-phase of the intermediate state can be formed a hollow 3D structure due to the release of ammonia gas, when exposed to 150 Pa.[19,29] The liquid-phase of the intermediate state has closed contact with the entire surface of FTO, resulting a good cycling performance, which should be facilitated to the practical application of photoelectrodes.
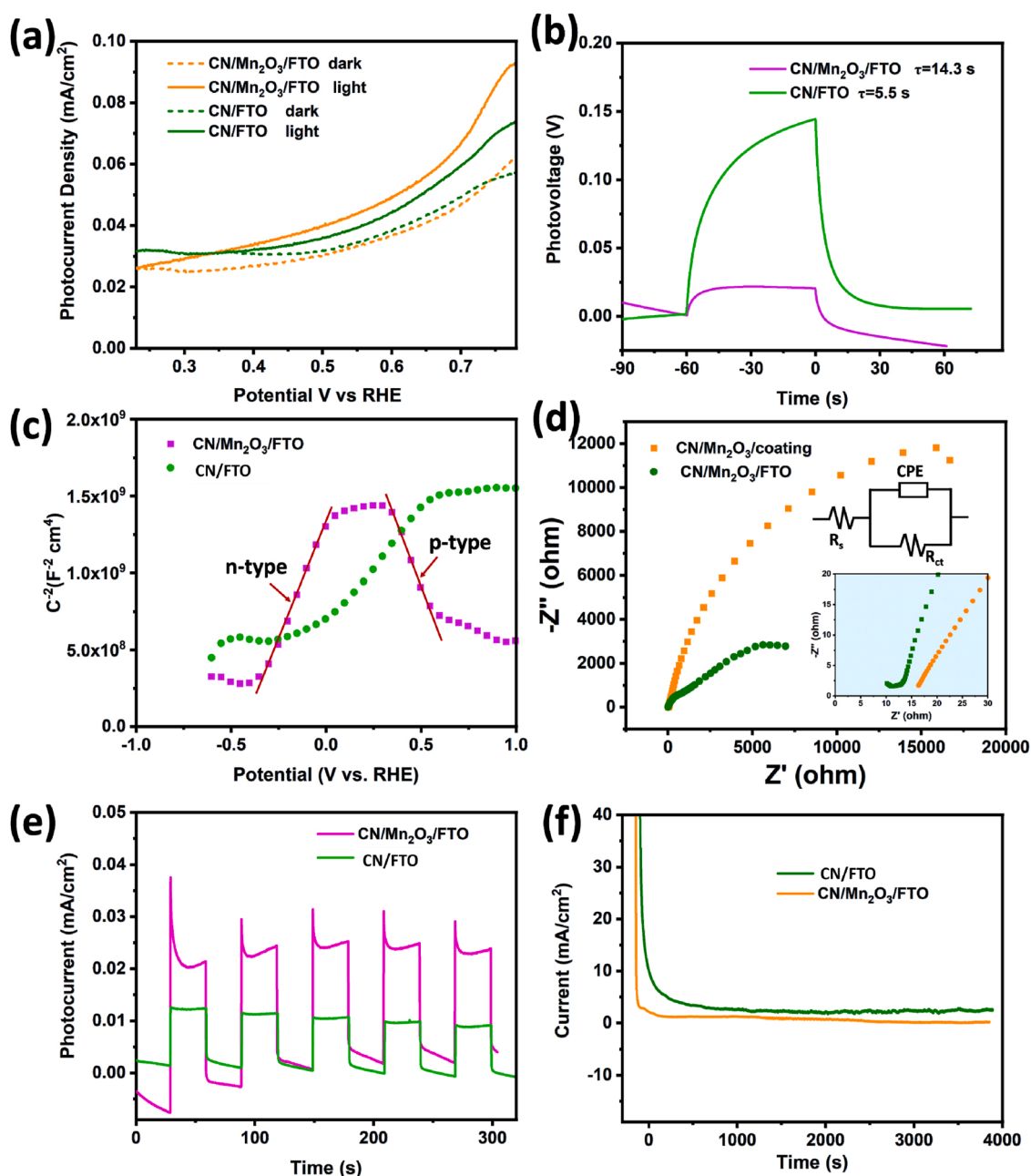

Fig. 4(. a) LSV curves, (b) Open circuit photovoltage decay (OCVD), and (c) Mott-Schottky plots of CN/Mn_2O_3/FTO and CN/FTO, (d) EIS Nyquist plots of CN/Mn_2O_3/FTO and CN/Mn_2O_3/coating, (e)Transient photocurrent responses, and (f) Chronoamperometry plot (i-t) of CN/Mn_2O_3/FTO and CN/FTO obtained in 0.1 M Na_2SO_4 (pH=6.5) electrolyte under irradiation of simulated sunlight.

3.2. The PEC performance of CN/Mn₂O₃/FTO p-n-heterojunction

To investigate the effect of plasma-assisted liquid-based growth method on photoelectrode of CN/Mn$_2$O$_3$/FTO, PEC measurements were implemented. Fig. 4(a) shows the LSV curves of CN/Mn$_2$O$_3$/FTO and CN/FTO samples. It can be seen that the CN/Mn$_2$O$_3$/FTO sample shows a clear photoanodic current with a low onset potential at + 0.23 V vs RHE. Such a low potential indicates that oxidation reaction is easily to occur at the electrode/electrolyte interface, possibly due to the accumulation of holes on the surface of semiconductor[39], resulting in a photoanode typical performance of about 93 μA/cm^2 at 0.8 V vs RHE. While the photocurrent density of CN/FTO photoelectrode is 74 μA/cm^2 with an onset potential at + 0.37 V vs RHE. The results indicate the formation of CN/Mn$_2$O$_3$ heterojunction could increase the surface hole accumulation, which can effectively improve the photocurrent density. [40].

The open circuit photovoltage decay (OCVD) was performed to gain insight into the mechanism behind the enhanced efficiency of PEC water splitting by plasma-assisted liquid-phase grown photoelectrodes. In Fig. 4(b), the photovoltage generated in CN/FTO is 7 times higher than that in CN/Mn$_2$O$_3$/FTO. This could be due to the band bending caused by the CN/Mn$_2$O$_3$ p-n heterojunction [39]. Moreover, the photoelectrons can accumulate at the defect state caused by N vacancies [41], leading to small photovoltages determined by the potential difference between trapped electron states and surface hole states. With careful observation of the OCVD, it can be seen that the photovoltage decay of CN/Mn$_2$O$_3$/FTO is much slower after illumination cut-off compared with CN/FTO. The average electron lifetimes of CN/Mn$_2$O$_3$/FTO and CN/FTO were determined to be 14.3 and 5.5 s, respectively, calculated by fitting the photovoltage decay curves. The observed average OCVD lifetime of CN/Mn$_2$O$_3$/FTO is 2.6 times longer than that of CN/FTO, which can be attributed to the residual surface N vacancy trapped electrons gradually recombining with the photogenerated holes in the bulk material that slowly diffusing to surface. In addition, it can be seen from Fig. S6 that the average OCVD lifetime of CN/Mn$_2$O$_3$/FTO-0.25, CN/Mn$_2$O$_3$/FTO-0.5, CN/Mn$_2$O$_3$/FTO-0.75 and CN/Mn$_2$O$_3$/FTO-1 are 8.9, 13.8, 14.3 and 10 s, respectively, indicating a critical effect of Mn$_2$O$_3$ on OCVD lifetime.

Fig. 4(c) shows the Mott-Schottky plots of CN/FTO and CN/Mn$_2$O$_3$/FTO in frequency range of 1000 Hz. The CN/FTO displays a positive slope, showing the behavior of n-type semiconductor. The positive slope touches the X-axis at a single point with three different frequencies ranges of 2000 Hz, 1000 Hz and 500 Hz shown in Fig. S7(a), which gives another support for the n-type behavior. In Fig. S7, the Mn$_2$O$_3$/FTO displays a negative slope, showing the behavior of p-type semiconductor. Besides, the CN/Mn$_2$O$_3$/FTO shows both positive and negative slopes, suggesting the formation of p-n-heterojunction owing to the p-type Mn$_2$O$_3$ semiconductor and n-type CN. MS analysis confirmed the formation of a p-n-heterojunction between p-type Mn$_2$O$_3$ and n-type CN semiconductors (Fig.S8, Supporting information). Moreover, the Fermi level can be estimated from the flat band potential of the semiconductor electrode. Compared to CN/FTO (−0.36 eV), the flat band potential of CN/Mn$_2$O$_3$/FTO (−0.45 eV) is negatively shifted, which means that Fermi levels are elevated. Such negative shift in the CB represents a higher and more unstable energy level of the electron.[42] As a result, electrons in the CB are more likely to be lost and oxidized. Combined with the XPS and EPR analysis discussed above, it is reasonable to speculate that N vacancy and the CN/Mn$_2$O$_3$/FTO p-n heterojunction may play a key role in their photoanode behavior. As for the solution, the particles in which are more likely to obtain the electrons in the semiconductor of CB, resulting in a photoreduction reactions. This is essential for photoelectrochemical water splitting.[43].

To investigate the photogenerated charge separation process at the electrolyte/electrode interface, the electrochemical impedance spectroscopy (EIS) was implemented. The impedance maps of the two photoelectrodes prepared by direct liquid-based growth and drop-coating

methods are displayed in Fig. 4(d) and analyzed in Table S4. The charge transfer resistance (R_{ct}) of CN/Mn$_2$O$_3$/FTO (3.5 × 10^1 Ω cm^2) is 2 orders of magnitude smaller than that of CN/Mn$_2$O$_3$/coating (1.7 × 10^3 Ω cm^2), which indicates the liquid-based growth photoelectrode has enhanced conductivity than that of drop-coating. Moreover, Fig. S9 displays CN/Mn$_2$O$_3$/FTO photoelectrodes with different Mn$_2$O$_3$ and CN/Mn$_2$O$_3$/FTO-0.75 shows a smallest arc radius which implies a faster charger transfer, indicating the addition of suitable Mn$_2$O$_3$ heterojunction onto CN leads to a decrease of the charge transfer resistance. [44].

Fig. 4(e) shows the transient photocurrent responses curves. As compared to the CN/FTO, the CN/Mn$_2$O$_3$/FTO exhibits a higher photocurrent density. The significantly enhanced photocurrent density is consistent with the observations in the EIS analysis. Comparing the photocurrents prepared by the liquid-based growth method and the drop-coating method, it can be found that the photocurrents obtained by the two methods have the same trend, and both CN/Mn$_2$O$_3$-0.75 has the highest photocurrent shown in Fig. S10, Supporting information. However, the photoelectrodes synthesized by liquid-based growth method have significantly increased photocurrent, which can be attributed to the liquid-based of the metastable state has closed contact with the entire surface of the substrate, which makes the photocarriers to be transferred quickly. Moreover, compared with the CN/Mn$_2$O$_3$/ITO photoelectrodes (Fig. S11), the CN/Mn$_2$O$_3$/FTO photoelectrodes show high photocurrent stability (Fig. 4(f) and Fig. S12), implying a great potential for practical PEC application. For practical applications, the cycle experiments were carried out for five successive reactions under the same conditions. The photocatalysts was washed with pure water and dried at 60 °C for ~12 hrs. In Fig. S13, the PEC value of CN/Mn$_2$O$_3$/FTO remained almost the same after five cycles experiments. Moreover, structural characterization of CN/Mn$_2$O$_3$/FTO was performed by XRD spectrum after cycling experiments. From Fig. S14 (Supporting Information), it can be concluded that the structure of CN/Mn$_2$O$_3$/FTO remains intact after five cycles PEC tests, indicating the stable structure.

3.3. Mechanism of photoelectrochemical water splitting

The nanosecond-level time-resolved fluorescence decay spectra were employed to investigate the charge transfer dynamics over CN/FTO and CN/Mn$_2$O$_3$/FTO series photoelectrodes (Fig. 5(a) and Fig. S15). The curve can be well fitted to a biexponential decay function, and all fitting parameters are summarized in Fig. S15, Supporting information. The prepared CN/Mn$_2$O$_3$/FTO series photoelectrodes are characterized by much lower average fluorescence lifetimes (1.83–2.53 ns) compared to CN/FTO (2.64 ns). The shortened lifetime suggests that the reduction of excited states in the prepared materials occurs more easily through a nonradiative pathway, presumably through charge transfer of electrons and holes to some favorable localized states, such as defect states, thus indicating improved charge separation. [45] The shorter decay time means faster transfer of photoexcited electrons in the composite photocatalyst electrode. Additionally, the recombination of photogenerated electron-hole pairs in the semiconductor was further investigate by PL spectra shown in Fig. 5(b). Compared to CN/FTO, the CN/Mn$_2$O$_3$/FTO exhibits weak fluorescence intensity, which can be explained by the inhibition of the recombination of photogenerated electrons and holes. The PL intensity decreases due to the nitrogen vacancy caused by the plasma treatment, resulting a new defect energy level.[46] The electrons at which are more easily excited, thus accelerates the separation of photogenic carriers. As for the "CN/Mn$_2$O$_3$/FTO" series photoelectrodes shown in Fig. S16, Supporting information, the CN/Mn$_2$O$_3$/FTO-0.75 displays a lowest PL intensity, which is well consistent with the results of its PEC performance analysis and fluorescence lifetimes analysis.

The optical absorption ability and band gap were investigated by the UV–visible absorption spectra shown in Fig. 5(c) and Fig. S17(a). The results showed that the absorption intensity of CN/Mn$_2$O$_3$/FTO increases due to the formation of p-n heterojunctions and plate
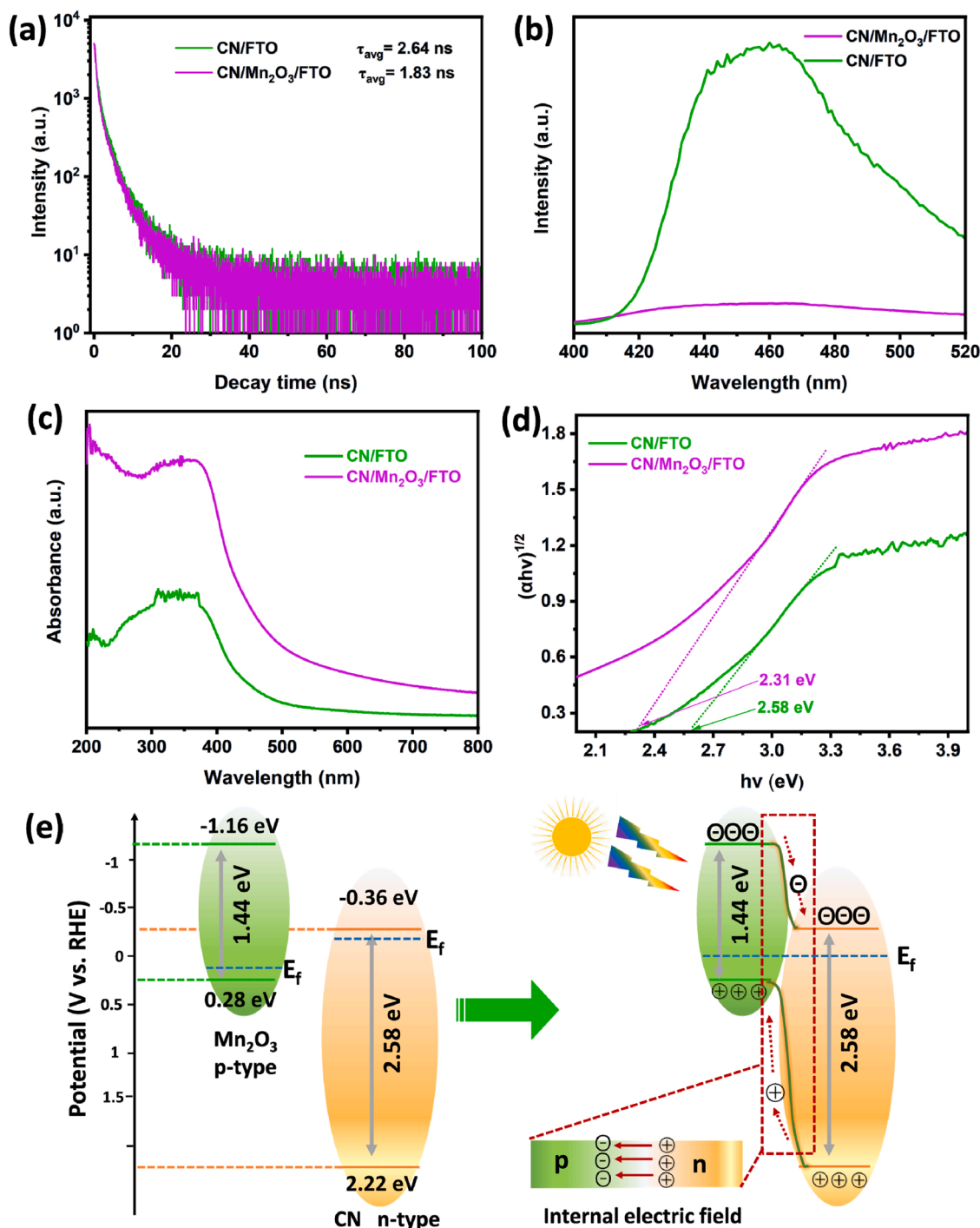
Fig. 5(. a) Nanosecond-level time-resolved fluorescence decay spectra, (b) the PL spectra, (c) the UV–visible absorption spectra, and (d) UV–visible diffuse reflectance spectroscopy of $CN/Mn_2O_3/FTO$ and CN/FTO, (e) Energy band structure of Mn_2O_3 and CN before and after contact and the possible charge transfer process for visible light-irradiated $CN/Mn_2O_3/FTO$ p-n heterojunction.

morphology as well as nitrogen vacancy when compared with CN/FTO. In Fig. 5(d), it can be suggested that the band gap of CN can be effectively adjusted by construction of Mn_2O_3 heterojunction. Importantly, it can be concluded that the heterojunction of Mn_2O_3 can realize the adjustable band gap of CN shown in Fig. S17(b). All these advantages features can benefit the enhancement of PEC performance for water splitting. Based on the results of MS analysis and UV–visible diffuse reflectance spectroscopy, the energy band structure was illustrated in Fig. S18, supporting information. All samples exhibited a more negative CB than •O- generation potential (−0.33 V vs NHE), indicating the

efficient reducing ability. Notably, the construction of the heterojunction can narrow the band gap of CN, but the position of CB is basically unchanged. This result implies that the construction of CN/Mn_2O_3 heterojunctions can realize tunable valence bands (VB).

Additionally, the Mn_2O_3/FTO was synthesized by the $KMnO_4$ reduction method [47] shown in supporting information. From the XRD spectrum (Fig. S19), the sample of Mn_2O_3/FTO shows the characteristic peaks of Mn_2O_3, which completely correspond to the PDF cards of Mn_2O_3, indicating that the Mn_2O_3/FTO photoelectrode was successfully prepared. In Fig. S20, it can be clearly obtained that the bandgap of

Mn_2O_3 is 1.44 eV. The VB of Mn_2O_3 can be obtained from the Mott-Schottky plot of Mn_2O_3/FTO (Fig. S7), which is 0.28 eV, thus the CB should be − 1.16 eV. According to the CB and VB obtained from Mn_2O_3 and CN, the energy band structure of semiconductor before contact was displayed in Fig. 5(e) (left). Typically, the Fermi level (E_f) is located near the CB position (negative about 0.10 eV) for n-type semiconductors and near VB for p-type semiconductors (positive about 0.10 eV). [48,49] The E_f values of Mn_2O_3 and CN are about 0.18 eV and 0.26 eV, respectively. Upon contact of these two semiconductors, electrons are transferred from CN (with higher E_f) to Mn_2O_3 (with lower E_f) until the two E_fs finally reach an equilibrium state. [50] This phenomenon will cause the energy band bending of the two semiconductors to form an internal electric field at the contact interface (Fig. 5(e), right). Driven by the internal electric field, the photogenerated electrons at the CB position of Mn_2O_3 are easily transferred to the CB position of CN, and the photogenerated holes are transferred from the VB of CN to the VB of Mn_2O_3. In this way, electrons and holes accumulate at the VB of CN and the CB of Mn_2O_3, respectively, which effectively separates photogenerated electron-hole pairs. Therefore, the Mn_2O_3/CN p-n heterojunction effectively retards the recombination of photogenerated electrons and holes, which is confirmed by the above PL and EIS Nyquist results.

The in-situ XPS measurement was used to explore the transfer route of photogenerated carriers under UV light illumination and the relative results are displayed in Fig. 6a–d. As shown, the C 1 s (C-NHx) peak after exposure exhibits higher binding energies compared to the values detected in the dark. For the peaks of N 1 s, a transition to lower binding energies is observed, indicating that N gains electrons. In addition, a new generation of Mn^{4+} peak was observed in Mn 2p (Fig. 6d), indicating that Mn lost electrons. In-situ XPS results show that the photogenerated electrons are transferred from Mn_2O_3 to CN, and the photogenerated holes are transferred from CN to Mn_2O_3, which is consistent with the results caused by the internal electric field at the interface of p-n heterojunction in Fig. 5(e). Thus, a possible mechanism of charge migration under photoelectrochemical reaction system is proposed in Fig. 6(e). Under the visible light irradiation, the CN/Mn_2O_3 is excited to generate the electrons (e⁻) and holes (h⁺). The photogenerated electros are transferred to the substrate of FTO, and further transferred to external circuit. More specially, a large number of Mn sites with various oxidation states in Mn_2O_3, which plays an important role in the photocatalytic reaction.[51] More detailly, the Mn^{3+} extracts holes from CN and is oxidized to Mn^{4+} when participated in water oxidation. Subsequently, the Mn^{4+} is returned to the original Mn^{3+} states.[52] In addition, the N vacancies also play a crucial role for water oxidation. In one hand, the N vacancies can promote charge separation and transfer the holes to the interfaces of anode to occur reaction.[53] In another
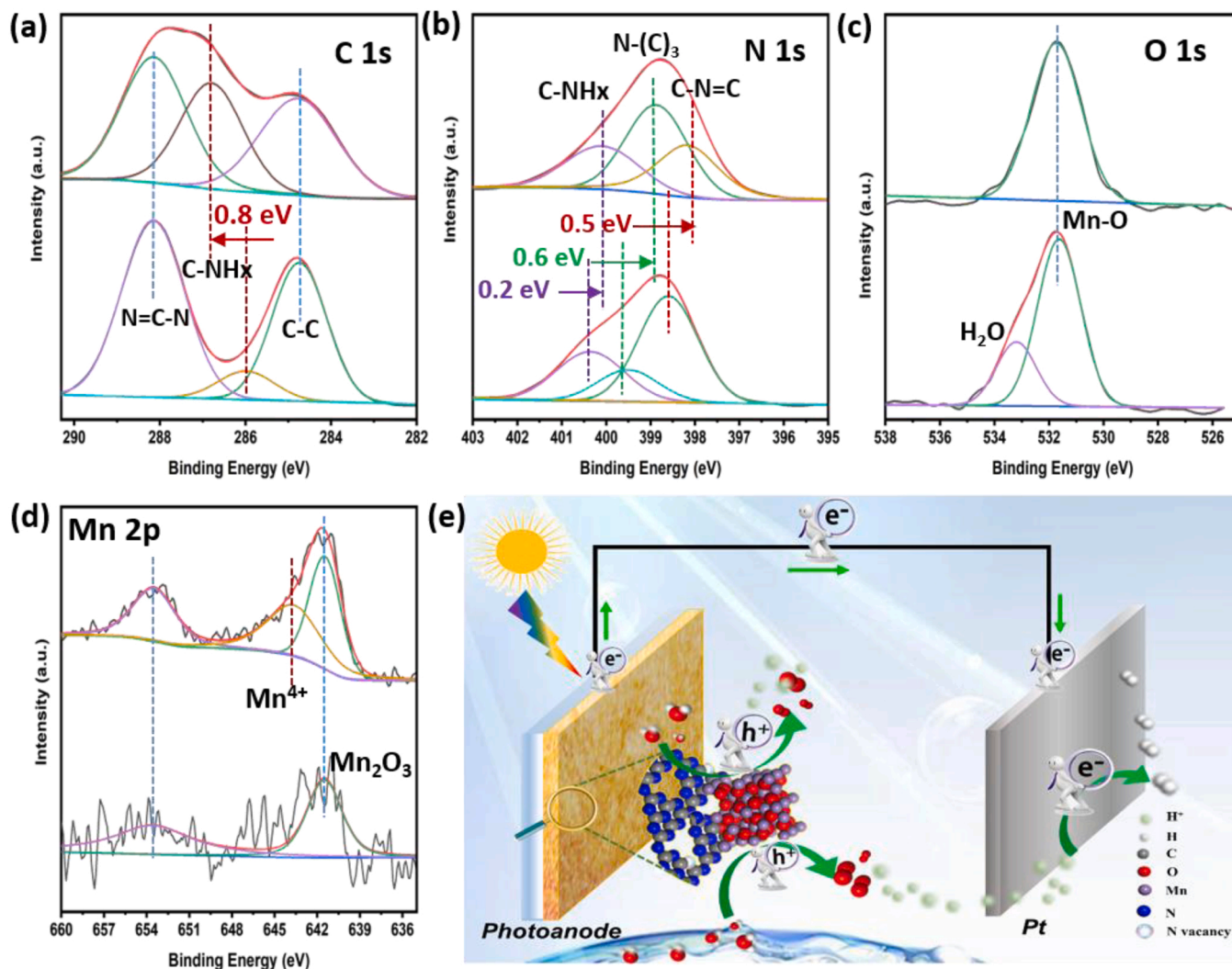

Fig. 6. In-situ XPS spectra of (a) C 1 s, (b)N 1 s, (c) O 1 s, and (d) Mn 2p for CN/Mn_2O_3/FTO (The above spectra were recorded under in-situ UV light irradiation for 10 min using xenon lamp, the spectra below were under dark conditions); (e)Schematic illumination of charge migration for CN/Mn_2O_3/FTO p-n heterojunction in photoelectrochemical reaction system.

hand, the defects of N vacancies can provide more active site to water oxidation.

4. Conclusion

In summary, we have directly grown a high-performance CN/Mn_2O_3/FTO p-n heterojunction by a plasma-assisted liquid-based thermal condensation method using MCS precursor on FTO substrate. The as-grown CN/Mn_2O_3/FTO p-n heterojunction is stable with excellent mechanical strength and exhibits a significantly enhanced PEC performance, and a tunable valence band (VB) attributed to the narrow bandgap of Mn_2O_3, which can facilitate the photocatalytic oxidation reaction. The internal electric field at the interface of p-n heterojunction can promote the transfer of photoelectrons, and lead to the accumulation of electrons and holes in the VB of CN and conduction band of Mn_2O_3. The results have shed a light on promoting the practical application of CN, and the developed plasma-assisted liquid-based growth method can be extended to the preparation of other type of functional heterojunctions.

CRediT authorship contribution statement

Yanmei Zheng: Formal analysis, Conceptualization, Writing – review & editing, Data curation, Investigation, Methodology. **Qiushi Ruan:** Investigation, Analysis of research results. **JingXuan Ren**: Investigation, Analysis of research results. **Xinli Guo:** Designer of the experiment, Editing, Supervision. **Yong Zhou**: Designer of the experiment, Editing. **Boye Zhou:** Analysis of research results. **Qiang Xu:** Methodology. **Qiuping Fu:** Analysis of research results. **Shaohua Wang:** Analysis of research results. **Ying Huang:** Writing – review & editing.

Declaration of Competing Interest

The authors declare that they have no known competing financial interests or personal relationships that could have appeared to influence the work reported in this paper.

Data Availability

No data was used for the research described in the article.

Acknowledgments

Appendix A. Supporting information

Supplementary data associated with this article can be found in the online version at doi:10.1016/j.apcatb.2022.122170.

References

[1] S. Yoshino, T. Takayama, Y. Yamaguchi, A. Iwase, A. Kudo, CO_2 reduction using water as an electron donor over heterogeneous photocatalysts aiming at artificial photosynthesis, Acc. Chem. Res. 55 (2022) 966–977.

[2] A. Landman, H. Dotan, G.E. Shter, M. Wullenkord, A. Houaijia, A. Maljusch, G.S. Grader, A. Rothschild, Photoelectrochemical water splitting in separate oxygen and hydrogen cells, Nat. Mater. 16 (2017) 646–651.

[3] K.P. Sokol, W.E. Robinson, J. Warnan, N. Kornienko, M.M. Nowaczyk, A. Ruff, J.Z. Zhang, E. Reisner, Bias-free photoelectrochemical water splitting with photosystem II on a dye-sensitized photoanode wired to hydrogenase, Nat. Energy 3 (2018) 944–951.

[4] X. Shi, H. Jeong, S.J. Oh, M. Ma, K. Zhang, J. Kwon, I.T. Choi, I.Y. Choi, H.K. Kim, J.K. Kim, J.H. Park, Unassisted photoelectrochemical water splitting exceeding 7%

[5] solar-to-hydrogen conversion efficiency using photon recycling, Nat. Commun. 7 (2016) 11943.

[5] B. Turan, J.P. Becker, F. Urbain, F. Finger, U. Rau, S. Haas, Upscaling of integrated photoelectrochemical water-splitting devices to large areas, Nat. Commun. 7 (2016) 12681.

[6] X. Chen, J. Wang, Y. Chai, Z. Zhang, Y. Zhu, Efficient photocatalytic overall water splitting induced by the giant internal electric field of a g-C_3N_4 /rGO/PDIP Z-scheme heterojunction, Adv. Mater. (2021), e2007479.

[7] C. Wu, S. Xue, Z. Qin, M. Nazari, G. Yang, S. Yue, T. Tong, H. Ghasemi, F.C. Hernandez, S. Xue, D. Zhang, H. Wang, Z.M. Wang, S. Pu, J. Bao, Making g-C_3N_4 ultra-thin nanosheets active for photocatalytic overall water splitting, Appl. Catal. B 282 (2021).

[8] P. Wen, Y. Sun, H. Li, Z. Liang, H. Wu, J. Zhang, H. Zeng, S.M. Geyer, L. Jiang, A highly active three-dimensional Z-scheme ZnO/Au/g-C_3N_4 photocathode for efficient photoelectrochemical water splitting, Appl. Catal. B 263 (2020).

[9] M. Kaur, M. Chhetri, C.N.R. Rao, Photoelectrochemical OER activity by employing BiVO4 with manganese oxide co-catalysts, Phys. Chem. Chem. Phys. 22 (2020) 811–817.

[10] F. Bi, Y. Su, Y. Zhang, M. Chen, J.A. Darr, X. Weng, Z. Wu, Vacancy-defect semiconductor quantum dots induced an S-scheme charge transfer pathway in 0D/2D structures under visible-light irradiation, Appl. Catal., B 306 (2022).

[11] H.S. Moon, K.C. Hsiao, M.C. Wu, Y. Yun, Y.J. Hsu, K. Yong, Spatial separation of cocatalysts on Z-scheme organic/inorganic heterostructure hollow spheres for enhanced photocatalytic H_2 evolution and in-depth analysis of the charge-transfer mechanism, Adv. Mater. (2022), e2200172.

[12] Y. Wei, L. Chen, H. Chen, L. Cai, G. Tan, Y. Qiu, Q. Xiang, G. Chen, T.C. Lau, M. Robert, Highly efficient photocatalytic reduction of CO_2 to CO by in situ formation of a hybrid catalytic system based on molecular iron quaterpyridine covalently linked to carbon nitride, Angew. Chem. Int. Ed. 61 (2022), e202116832.

[13] B. He, S. Zhang, Y. Zhang, G. Li, B. Zhang, W. Ma, B. Rao, R. Song, L. Zhang, Y. Zhang, G. He, Ortho-Terphenylene viologens with through-space conjugation for enhanced photocatalytic oxidative coupling and hydrogen evolution, J. Am. Chem. Soc. 144 (2022) 4422–4430.

[14] W. He, L. Liu, T. Ma, H. Han, J. Zhu, Y. Liu, Z. Fang, Z. Yang, K. Guo, Controllable morphology CoFe$_2$O$_4$/g-C_3N_4 p-n heterojunction photocatalysts with built-in electric field enhance photocatalytic performance, Appl. Catal. B 306 (2022).

[15] Y. Zheng, Y. Luo, Q. Ruan, S. Wang, J. Yu, X. Guo, W. Zhang, H. Xie, Z. Zhang, Y. Huang, Plasma-induced hierarchical amorphous carbon nitride nanostructure with two N_2 C-site vacancies for photocatalytic H_2O_2 production, Appl. Catal., B 311 (2022).

[16] J. Ding, Q. Tang, Y. Fu, Y. Zhang, J. Hu, T. Li, Q. Zhong, M. Fan, H.H. Kung, Core-shell covalently linked graphitic carbon nitride-melamine-resorcinol-formaldehyde microsphere polymers for efficient photocatalytic CO_2 reduction to methanol, J. Am. Chem. Soc. 144 (2022) 9576–9585.

[17] D. Li, C. Wen, J. Huang, J. Zhong, P. Chen, H. Liu, Z. Wang, Y. Liu, W. Lv, G. Liu, High-efficiency ultrathin porous phosphorus-doped graphitic carbon nitride nanosheet photocatalyst for energy production and environmental remediation, Appl. Catal. B 307 (2022).

[18] X. Liu, J. Wang, D. Wu, Z. Wang, Y. Li, X. Fan, F. Zhang, G. Zhang, W. Peng, N-doped carbon dots decorated 3D g-C_3N_4 for visible-light driven peroxydisulfate activation: Insights of non-radical route induced by Na+ doping, Appl. Catal. B 310 (2022).

[19] J. Bian, Q. Li, C. Huang, J. Li, Y. Guo, M. Zaw, R.-Q. Zhang, Thermal vapor condensation of uniform graphitic carbon nitride films with remarkable photocurrent density for photoelectrochemical applications, Nano Energy 15 (2015) 353–361.

[20] J. Liu, H. Wang, Z.P. Chen, H. Moehwald, S. Fiechter, R. van de Krol, L. Wen, L. Jiang, M. Antonietti, Microcontact-printing-assisted access of graphitic carbon nitride films with favorable textures toward photoelectrochemical application, Adv. Mater. 27 (2015) 712–718.

[21] M. Shalom, S. Gimenez, F. Schipper, I. Herraiz-Cardona, J. Bisquert, M. Antonietti, Controlled carbon nitride growth on surfaces for hydrogen evolution electrodes, Angew. Chem. Int. Ed. 53 (2014) 3654–3658.

[22] M.-W. Kim, B. Joshi, E. Samuel, H. Seok, A. Aldalbahi, M. Almoiqli, M.T. Swihart, S.S. Yoon, Electrosprayed MnO$_2$ on ZnO nanorods with atomic layer deposited TiO$_2$ layer for photoelectrocatalytic water splitting, Appl. Catal., B 271 (2020).

[23] I. Zaharieva, P. Chernev, M. Risch, K. Klingan, M. Kohlhoff, A. Fischer, H. Dau, Electrosynthesis, functional, and structural characterization of a water-oxidizing manganese oxide, Energy Environ. Sci. 5 (2012).

[24] M.M. Kandy, V.G. Gaikar, Enhanced photocatalytic reduction of CO_2 using CdS/Mn_2O_3 nanocomposite photocatalysts on porous anodic alumina support with solar concentrators, Renew. Energy 139 (2019) 915–923.

[25] R. Naeem, M. Ali Ehsan, R. Yahya, M. Sohail, H. Khaledi, M. Mazhar, Fabrication of pristine Mn_2O_3 and Ag-Mn_2O_3 composite thin films by AACVD for photoelectrochemical water splitting, Dalton Trans. 45 (2016) 14928–14939.

[26] Y. Gorlin, C.-J. Chung, D. Nordlund, B.M. Clemens, T.F. Jaramillo, Mn3O4 supported on glassy carbon: an active non-precious metal catalyst for the oxygen reduction reaction, ACS Catal. 2 (2012) 2687–2694.

[27] X. Zhang, Y. Liu, L. Chen, Z. Li, Y. Qu, W. Wu, L. Jing, Porous two-dimension MnO$_2$-C$_3$N$_4$/titanium phosphate nanocomposites as efficient photocatalysts for CO oxidation and mechanisms, Appl. Catal. B 282 (2021).

[28] J. Zhao, N. Li, R. Yu, Z. Zhao, J. Nan, Magnetic field enhanced denitrification in nitrate and ammonia contaminated water under 3D/2D Mn_2O_3/g-C$_3$N$_4$ photocatalysis, Chem. Eng. J. 349 (2018) 530–538.

[29] X. Lu, Z. Liu, J. Li, J. Zhang, Z. Guo, Novel framework g-C3N4 film as efficient photoanode for photoelectrochemical water splitting, Appl. Catal., B 209 (2017) 657–662.

[30] J. Zhao, J. Nan, Z. Zhao, N. Li, Facile fabrication of novel Mn_2O_3 nanocubes with superior light-harvesting for ciprofloxacin degradation, Catal. Commun. 102 (2017) 5–8.

[31] Y. Geng, D. Chen, N. Li, Q. Xu, H. Li, J. He, J. Lu, Z-Scheme 2D/2D α-Fe_2O_3/g-C3N4 heterojunction for photocatalytic oxidation of nitric oxide, Appl. Catal., B 280 (2021).

[32] J. Xu, T.J. Brenner, L. Chabanne, D. Neher, M. Antonietti, M. Shalom, Liquid-based growth of polymeric carbon nitride layers and their use in a mesostructured polymer solar cell with V(oc) exceeding 1 V, J. Am. Chem. Soc. 136 (39) (2014) 13486–13489.

[33] G. Peng, J. Albero, H. Garcia, M. Shalom, A water-splitting carbon nitride photoelectrochemical cell with efficient charge separation and remarkably low onset potential, Angew. Chem. Int. Ed. Engl. 57 (48) (2018) 15807–15811.

[34] X. Lv, M. Cao, W. Shi, M. Wang, Y. Shen, A new strategy of preparing uniform graphitic carbon nitride films for photoelectrochemical application, Carbon 117 (2017) 343–350.

[35] D. Zhu, Q. Zhou, Nitrogen doped g-C3N4 with the extremely narrow band gap for excellent photocatalytic activities under visible light, Appl. Catal., B 281 (2021).

[36] X. Qu, S. Hu, P. Li, Z. Li, H. Wang, H. Ma, W. Li, The effect of embedding N vacancies into g-C3N4 on the photocatalytic H_2O_2 production ability via H_2 plasma treatment, Diam. Relat. Mater. 86 (2018) 159–166.

[37] X. Ji, X. Yuan, J. Wu, L. Yu, H. Guo, H. Wang, H. Zhang, D. Yu, Y. Zhao, Tuning the Photocatalytic Activity of Graphitic Carbon Nitride by Plasma-Based Surface Modification, ACS Appl. Mater. Interfaces 9 (29) (2017) 24616–24624.

[38] G. Yang, Y. Kuwahara, K. Mori, C. Louis, H. Yamashita, PdAg alloy nanoparticles encapsulated in N-doped microporous hollow carbon spheres for hydrogenation of CO_2 to formate, Appl. Catal., B 283 (2021).

[39] Q. Ruan, T. Miao, H. Wang, J. Tang, Insight on shallow trap states-introduced photocathodic performance in n-type polymer photocatalysts, J. Am. Chem. Soc. 142 (6) (2020) 2795–2802.

[40] S.O. Ganiyu, M.J.G. de Araújo, E.C.T. de Araújo Costa, J.E.L. Santos, E.V. dos Santos, C.A. Martínez-Huitle, S.B.C. Pergher, Design of highly efficient porous carbon foam cathode for electro-Fenton degradation of antimicrobial sulfanilamide, Appl. Catal. B 283 (2021).

[41] Y. Zheng, Y. Luo, Q. Ruan, J. Yu, X. Guo, W. Zhang, H. Xie, Z. Zhang, J. Zhao, Y. Huang, Plasma-Tuned nitrogen vacancy graphitic carbon nitride sphere for

[42] Y. Yang, B. Hu, W. Zhao, Q. Yang, F. Yang, J. Ren, X. Li, Y. Jin, L. Fang, Q. Pan, Bridging N-doped graphene and carbon rich C3N4 layers for photo-promoted multi-functional electrocatalysts, Electrochim. Acta 317 (2019) 25–33.

[43] C. Ling, X. Niu, Q. Li, A. Du, J. Wang, Metal-free single atom catalyst for N_2 fixation driven by visible light, J. Am. Chem. Soc. 140 (43) (2018) 14161–14168.

[44] Z. Teng, W. Cai, W. Sim, Q. Zhang, C. Wang, C. Su, T. Ohno, Photoexcited single metal atom catalysts for heterogeneous photocatalytic H_2O_2 production: pragmatic guidelines for predicting charge separation, Appl. Catal., B 282 (2021).

[45] Z. Chen, A. Savateev, S. Pronkin, V. Papaefthimiou, C. Wolff, M.G. Willinger, E. Willinger, D. Neher, M. Antonietti, D. Dontsova, "The easier the better" preparation of efficient photocatalysts-metastable poly(heptazine imide) salts, Adv. Mater. 29 (32) (2017).

[46] J. Ma, D. Jin, Y. Li, D. Xiao, G. Jiao, Q. Liu, Y. Guo, L. Xiao, X. Chen, X. Li, J. Zhou, R. Sun, Photocatalytic conversion of biomass-based monosaccharides to lactic acid by ultrathin porous oxygen doped carbon nitride, Appl. Catal., B 283 (2021).

[47] Q. Tang, L. Jiang, J. Liu, S. Wang, G. Sun, Effect of surface manganese valence of manganese oxides on the activity of the oxygen reduction reaction in alkaline media, ACS Catal. 4 (2) (2014) 457–463.

[48] S. Saha, G. Das, J. Thote, R. Banerjee, Photocatalytic metal-organic framework from CdS quantum dot incubated luminescent metallohydrogel, J. Am. Chem. Soc. 136 (42) (2014) 14845–14851.

[49] Y. Jia, J. Yang, D. Zhao, H. Han, C. Li, A. Novel, Sr_2CuInO_3S p-type semiconductor photocatalyst for hydrogen production under visible light irradiation, J. Energy Chem. 23 (4) (2014) 420–426.

[50] Y. Huang, D. Zhu, Q. Zhang, Y. Zhang, J.-J. Cao, Z. Shen, W. Ho, S.C. Lee, Synthesis of a $Bi_2O_2CO_3$/$ZnFe_2O_4$ heterojunction with enhanced photocatalytic activity for visible light irradiation-induced NO removal, Appl. Catal. B 234 (2018) 70–78.

[51] I. Zaharieva, M.M. Najafpour, M. Wiechen, M. Haumann, P. Kurz, H. Dau, Synthetic manganese–calcium oxides mimic the water-oxidizing complex of photosynthesis functionally and structurally, Energy Environ. Sci. 4 (7) (2011).

[52] X. Cheng, G. Dong, Y. Zhang, C. Feng, Y. Bi, Dual-bonding interactions between MnO2cocatalyst and TiO2 photoanodes for efficient solar water splitting, Appl. Catal., B 267 (2020).

[53] M.H. Elsayed, J. Jayakumar, M. Abdellah, T.H. Mansoure, K. Zheng, A.M. Elewa, C.-L. Chang, L.-Y. Ting, W.-C. Lin, H.-H. Yu, W.-H. Wang, C.-C. Chung, H.-H. Chou, Visible-light-driven hydrogen evolution using nitrogen-doped carbon quantum dot-implanted polymer dots as metal-free photocatalysts, Appl. Catal. B 283 (2021).